Applied Physics Letters

Epitaxial type-I and type-II InAs-AlAsSb core–shell nanowires on silicon

Cite as: Appl. Phys. Lett. **119**, 193102 (2021); https://doi.org/10.1063/5.0065867
Submitted: 05 August 2021 • Accepted: 23 October 2021 • Published Online: 08 November 2021

Fabio del Giudice, Sergej Fust, Paul Schmiedeke, et al.

Applied Physics Letters ARTICLE scitation.org/journal/apl

Epitaxial type-I and type-II InAs-AlAsSb core–shell nanowires on silicon

Cite as: Appl. Phys. Lett. **119**, 193102 (2021); doi: 10.1063/5.0065867
Submitted: 5 August 2021 · Accepted: 23 October 2021 ·
Published Online: 8 November 2021

Fabio del Giudice,[1] Sergej Fust,[1] Paul Schmiedeke,[1] Johannes Pantle,[1] Markus Döblinger,[2] Akhil Ajay,[1] Steffen Meder,[1] Hubert Riedl,[1] Jonathan J. Finley,[1] and Gregor Koblmüller[1,a)]

AFFILIATIONS

[1]Walter Schottky Institute and Physics Department, Technical University of Munich, Garching 85748, Germany
[2]Department of Chemistry, Ludwig-Maximilians-University Munich, Munich 81377, Germany

[a)]Author to whom correspondence should be addressed: Gregor.Koblmueller@wsi.tum.de

ABSTRACT

Low-bandgap semiconductor nanowires (NWs) attract considerable interest for mid-infrared (MIR) photonics and optoelectronics, where ideal candidate materials require surface-passivated core–shell systems with large tunability in band offset, lineup, and emission wavelength while maintaining close lattice-matching conditions. Here, we propose and demonstrate epitaxial InAs–AlAsSb core–shell NW arrays on silicon (Si) that offer exceptional control over both the internal strain close to lattice-matching as well as band lineups tunable between type-I and type-II, with almost no analogue in the III–V materials family. We develop direct monolithic growth of high-uniformity InAs–AlAsSb NWs with wide tunability in shell composition and employ correlated Raman scattering and micro-photoluminescence spectroscopy to elaborate the interplay among hydrostatic strain, band lineup, and emission energy of the NW core luminescence tuned from ~0.4 to 0.55 eV. Electronic structure calculations further support the experimentally observed tunability between type-I and type-II band lineups. The Si-integrated InAs-AlAsSb NW materials system holds large prospects not only for on-chip MIR photonics but also for other applications including high-speed transistors and NW-based hot carrier solar cells.

Low-bandgap InAs nanowires (NWs) have drawn much attention in recent years due to their potential applications in electronics, photonics, and mid-infrared (MIR) optoelectronics. Their high electron mobility, large absorption coefficient, and narrow direct bandgap make them predestined materials for high-speed transistors,[1,2] nano-thermoelectric devices[3,4] as well as photodetectors,[5] MIR light sources such as lasers,[6,7] and THz emitters.[8] The possibility of direct monolithic integration on Si displays them as attractive candidates for forthcoming technological applications in MIR Si-photonics and lab-on-chip optoelectronics.[9,10]

However, InAs NWs are commonly plagued by defect states and Fermi level pinning at the surface.[11] Nowadays, this can be effectively overcome by suitable encapsulating passivation layers to enhance the carrier mobility and carrier lifetime[12–14] and improve luminescence efficiencies by reducing non-radiative surface recombination.[14,15] So far, these prominent effects were mainly demonstrated in few core–shell NW systems, where the InAs core was passivated with, e.g., epitaxial InAlAs[12,13] or In(As)P[14,16] shell layers. These core-shell systems suffer though from two essential drawbacks. First, InAlAs and InAsP exhibit large lattice mismatches with the core, bearing the risk for strain-induced defect formation. This limits the shell growth to very thin layers and low tunability in shell composition,[17] preventing flexibility in electronic band engineering and the realization of functional core-multishell NW devices where extended shell thicknesses are required, as in, e.g., NW-lasers,[18] radial NW-solar cells,[19] or modulation-doped NW-transistors.[20] Second, these conventional shell systems are limited to type-I band lineup between the core and shell, as in most traditional III–V semiconductors. However, there are many intriguing optoelectronic applications of InAs NWs where type-II band lineup is much preferred, for example, in type-II MIR sources with suppressed Auger recombination[21,22] and hot-carrier solar cells, in which efficient spatial separation of carriers is crucial.[23]

Against this backdrop, we develop here a unique InAs-AlAsSb core-shell NW system allowing close lattice-matching properties and exceptional tunability in band lineups from type-I to type-II, as not reported before. As a member of the "6.1 Å" family of materials, the InAs/AlAsSb stands out for its exceptionally high conduction band offset (up to 1.35 eV) and excellent electron confinement with no

counterpart among all III–V semiconductors.[24] Especially, we pioneer the monolithic integration of high-uniformity, composition-tunable InAs/AlAsSb NW arrays on Si and explore systematically the effects of shell composition on the morphological, strain, and optical properties using correlated Raman and micro-photoluminescence (μPL) spectroscopy. Supported by strain and electronic structure calculations, we directly highlight the tunability between type-I and type-II band lineups in these core-shell NWs, illustrating their versatility for widespread nanoscale Si-photonic and optoelectronic applications.

The NWs were grown by selective-area molecular beam epitaxy (SA-MBE) using common effusion cells for group III elements and two valve cracker cells providing uncracked As_4 and cracked Sb_2, respectively. Commercial Si (111) wafers with a 20-nm thick thermally grown SiO_2 mask layer on top served as epitaxial substrates. Hereby, the SiO_2 layer was prepatterned by electron beam lithography, reactive ion etching, and a buffered oxide etch [BOE:98:2 NH_4F(40%):HF(50%)] to induce site selective NW growth from periodic openings with diameters of ~140 nm.[25–27] InAs NW cores were grown at 520 °C for 60 min with an In flux of 0.6 Å/s and an As_4 beam equivalent pressure (BEP) of 4.5×10^{-5} mbar, corresponding to a V/III ratio of ~40.[25] These parameters result in catalyst-free, i.e., vapor-solid type NWs with lengths of ~8 μm and diameters of ~210 nm [see Fig. 1(a)], and a typical wurtzite (WZ)-phase microstructure with high stacking fault densities[26,27] (see the supplementary material). After core growth, a ~30 min pause was set to remove residual As from the background environment (avoiding unintentional As deposition) and to lower the temperature to 425 °C for subsequent AlAsSb shell growth. AlAsSb shells were grown for 30 min at an Al flux of 0.5 Å/s (equivalent planar growth rate), Sb_2 BEP of 1.2×10^{-6} mbar, while the As_4 BEP was varied between 2×10^{-7} and 2×10^{-6} mbar to tune the As fraction in different samples. All respective fluxes were supplied at the same time to initiate AlAsSb shell growth. To prevent oxidation of the AlAsSb layer, a GaSb cap was grown for 10 min under a Ga flux of 0.5 Å/s and a Sb_2 BEP of 1.2×10^{-6} mbar.

Figure 1(a) shows typical scanning electron microscopy (SEM) images of as-grown InAs–core and InAs–AlAsSb core–shell NW arrays in comparison. The NW arrays exhibit exceptional uniformity with very high epitaxial growth yield,[25,26] yet, a non-flat, pencil-like NW tip that is common under the employed SA-MBE growth.[28] Since the NW cores were grown under the exactly same conditions, the NW lengths remain unchanged in the core-shell NWs (~8 μm), while only the NW diameter is increased. Also note that both the core-only and core–shell NWs have straight sidewalls, indicating a homogeneous and taper-free growth along the entire NW length. This is in distinct contrast to previous growth attempts of core-shell NWs with binary AlSb shells, which exhibited non-epitaxial orientation and strong NW bending due to inhomogeneous shell growth.[29,30] The total diameter of our core-shell NWs is ~260 (±20) nm, corresponding to an AlAsSb shell (GaSb cap) thickness of ~20 nm (5 nm), irrespective of the supplied As flux [Fig. 1(b)]. This suggests that the shell growth is limited by the available Al flux, which in a coaxial NW geometry is ~1/5 of the group-III limited planar growth rate.[31] The shell thickness and its coherent growth around the NW core were further confirmed by transmission electron microscopy (TEM) measurements (see the supplementary material).

A closer view at the surface morphology for shells grown under different As fluxes is presented in Fig. 1(b). Here, we also show NWs

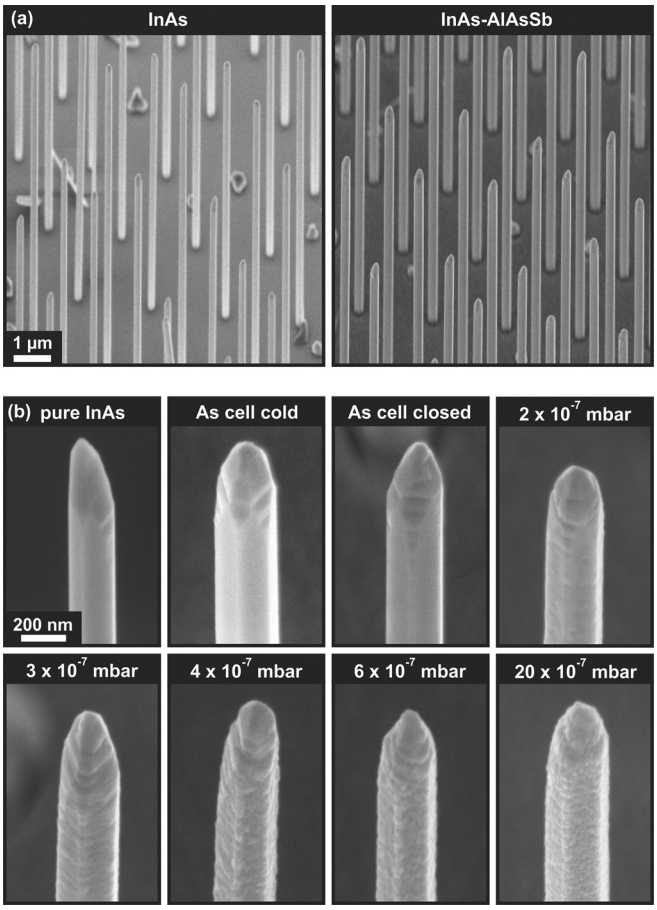

FIG. 1. (a) Overview SEM images taken from arrays of InAs NWs (left) and InAs–AlAsSb core–shell NWs (right) under 45° tilted view and with identical scale bar. (b) Close-up view of individual NWs illustrating the morphological evolution of the AlAsSb shell grown under different As-fluxes. The corresponding As-supply is given in the top panel for each image. The scale bar (200 nm) is the same for all images.

where shells were grown without active As supply, denoted as "As-closed" and "As-cold," respectively. These growths aim at pure AlSb layers, where "As-closed" refers to conditions with the closed As-cell kept at the operating temperature (380 °C) of the valved cracker, while "As-cold" describes similar conditions with the closed As-cell fixed at 250 °C standby temperature. Although these conditions provide no nominal As flux, miniscule amounts of residual As are incorporated (likely from a needle valve run without shutters), hampering the growth of pure AlSb shells as further shown below. Such Al(As)Sb shells exhibit specular NW sidewall morphology with very flat facets, similar to the bare InAs cores (top-left image). Adding a small As-flux of 2×10^{-7} mbar maintains overall smooth facet morphology, albeit some faint surface undulations (striated morphology) appear orthogonal to the growth axis. The striated morphology becomes even more pronounced for slightly increased As-flux (3×10^{-7} mbar). We assume that such morphology could result from growth instabilities, e.g., anisotropic adatom kinetics, under the presence of high stacking

fault densities, as seen in many other materials.[32–34] Furthermore, for higher As fluxes, the striated morphology transforms into a roughened, grainlike surface (3D islanding), where the density of grains increases rapidly with As-flux. Since high fractions of As in the AlAsSb shell lead to substantial lattice-mismatch with the core, the transition to such a 3D-grainlike structure can be linked to onsets of strain relaxation (shown in Fig. 3).

To characterize the composition and strain properties of the InAs-AlAsSb NWs, micro(μ)-Raman scattering spectroscopy was performed on individual NWs at room temperature. The measurements were performed in a confocal alpha300R WITec microscope, using an excitation laser with wavelength $\lambda = 532$ nm and a spot size of ~0.45 ($\pm$0.1) μm (100×/0.9 NA objective). The Raman signals were collected in backscattering geometry with normal incidence excitation on the sidewall facet of single NWs that had been dispersed onto a Si wafer. The measurements were performed without distinguishing the polarization of the phonon modes. In total, eight samples with different AlAsSb shell compositions were characterized, and 3–5 NWs/samples were probed to obtain statistically relevant data. Figure 2(a) presents Raman spectra (at 150 μW excitation power) of bare InAs NWs (gray) and core-shell NWs from the same samples as in Fig. 1(b), plotted as the arithmetic mean over the measured number of NWs/samples. In the case of bare InAs NWs, we observe the transverse optical (TO) phonons as the dominant mode with peak positions at ~216 cm^{-1}, in good agreement with reported values for WZ-phase InAs NWs.[35,36] A residuary feature is also shown at very low wavenumbers (<100 cm^{-1}) that stems most likely from the laser as it remains persistent in all samples. Additional residuary features are observed between ~100 and 150 cm^{-1} in the core-shell NWs (especially for the highest As-flux). These peaks might be associated with bulk Sb[37] and likely appear as a result of thermal decomposition of the AlAsSb shell upon irradiation by the high-energy excitation laser (see the supplementary material). Furthermore, the core-shell NWs exhibit a peak at ~227 cm^{-1}, which can be linked to the GaSb TO phonon mode of the 5-nm thin GaSb cap layer.[38]

Most importantly, the core–shell NWs show a very characteristic Raman peak at longer wavenumbers at ~320–350 cm^{-1} that obviously depends on the As flux during AlAsSb shell growth. This peak is attributed to the TO phonon mode of AlAsSb, since its Raman shift occurs continually with increasing As supply from close to the bulk AlSb TO resonance at ~319 cm^{-1} toward the AlAs TO resonance at ~361 cm^{-1}.[39–41] Hence, the shift of this TO mode reflects the change in alloy composition of the AlAsSb shell in the respective samples. Note that also a faint peak is observed near ~340 cm^{-1} (particularly in samples without intentional As supply), which is attributed to the AlSb LO phonon mode.[39,41] Interestingly, as the AlAsSb alloy

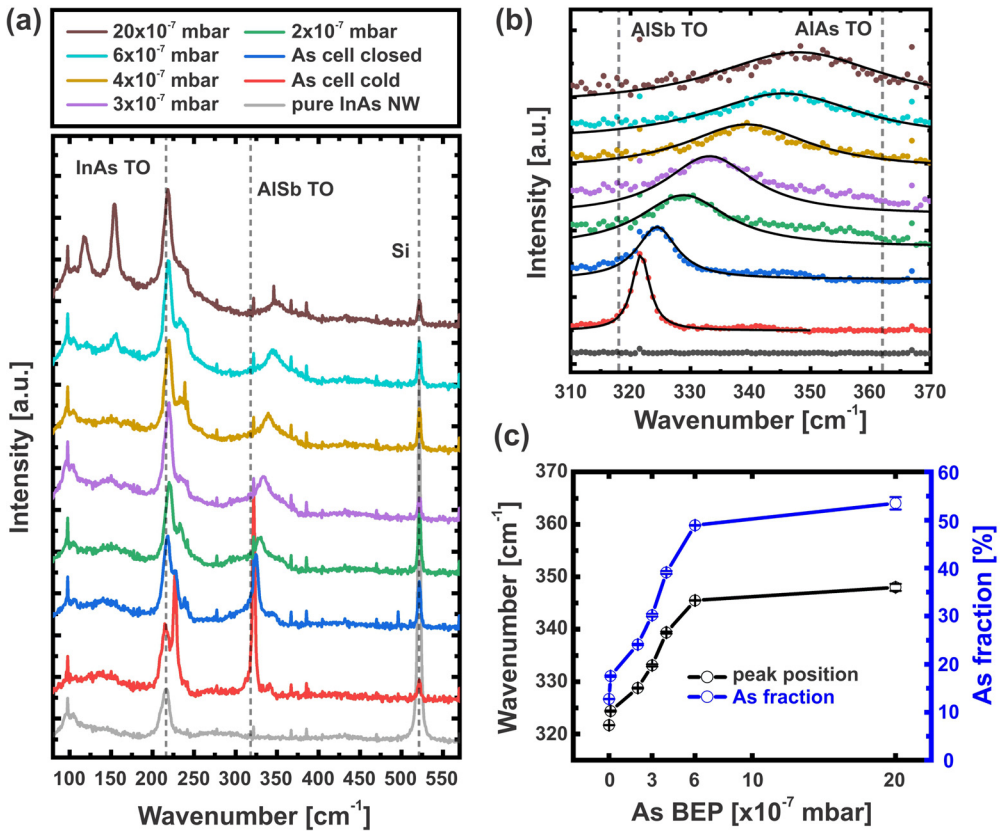

FIG. 2. (a) Raman spectra of InAs core-only (grey) and InAs–AlAsSb core–shell NWs recorded from the same samples as in Fig. 1. Spectra have been shifted vertically for clarity; (b) TO-phonon mode shift of the AlAsSb shell layer with increasing As-supply, showing experimental data together with Lorentzian peak fits (solid lines); (c) peak wavenumbers of the AlAsSb-related TO mode and corresponding As-fractions in the AlAsSb shell derived from the empirical model by Sela *et al.*[40]

composition is tuned throughout these samples, no further TO (or LO) modes appear, which is characteristic for a single-mode alloy and unique for AlAsSb.[40,41] In addition, the TO phonon peak broadens upon increasing the As flux, i.e., larger As incorporation. This likely reflects increased structural disorder as the lattice mismatch with the core rises toward As-rich AlAsSb shell layers (~7% mismatch in InAs/AlAs), in line with the increasingly roughened surface morphology in Fig. 1(b). Additionally, we cannot rule out alloy disorder effects to contribute to the peak broadening, as previously observed in the literature.[41,42]

By using Lorentzian fitting, the TO peak position and shift can be determined more accurately [see Figs. 2(b) and 2(c)]. Hereby, we find that for nominally As-free AlSb shell layers ("As-cold" and "As-closed"), the TO peak is centered at around 321 and 324 cm^{-1}, respectively. These values are slightly larger than the TO resonance for bulk AlSb and hint, therefore, toward small As incorporation. The TO mode shifts then with intentional As supply and appears to saturate near ~346 cm^{-1} for the highest selected As flux. This trend is directly reflected in the estimated alloy composition [Fig. 2(c)] that was derived from the non-linear relationship between the Raman shift and corresponding As molar fraction, as proposed by Sela *et al.* (assuming a zinc blende structure).[40] As a result, the As fraction in the AlAsSb shell layers ranges from ~13% to ~55%, where it saturates. We suspect that the apparent saturation stems from the low shell growth temperature, which favors the relative incorporation of Sb over As.[43]

Importantly, our data suggest that with the large tunability in shell composition and lattice mismatch, we should be able to tune the strain state, and its *sign*, of the InAs core, which is the most relevant parameter affecting the electronic and optical transition properties in these NWs. In particular, we expect to tune the strain in the core from a weakly *tensile* strain state (via a Sb-rich AlAsSb shell), over lattice-matching conditions, to a *compressive* strain state (via a more As-rich AlAsSb shell), providing powerful strain control in binary NWs that have very few analogs among the plethora of III–V semiconductors.

To demonstrate this, we focus now our analysis on the shift of the InAs TO phonon mode as a function of the AlAsSb shell composition, illustrated in the close-up view of Fig. 3(a). Note, the spectra of Sb-rich core–shell NWs resolve also more closely the Raman peak at ~227 cm^{-1} (the GaSb TO-mode) and further a weaker feature at ~236 cm^{-1}, which is ascribed to the GaSb LO-mode from the GaSb cap.[38] For more As-rich core-shell NWs, the GaSb TO-mode broadens and shifts to larger wavenumbers, which is likely due to residual As incorporating into the GaSb cap after AlAsSb shell growth. Most prominently, the InAs TO-mode shift shows a characteristic shape: first, with respect to bare strain-free InAs (216 cm^{-1}), a slight shift to lower wavenumbers for NWs containing Sb-rich AlAsSb shells is observed, which is followed by a shift to larger wavenumbers for less Sb-rich shells. For more As-rich AlAsSb shells, the shift inverts again toward lower wavenumbers. By determining the relative peak shifts ($\Delta\nu/\nu_{TO}$) with respect to the strain-free position of the InAs TO-

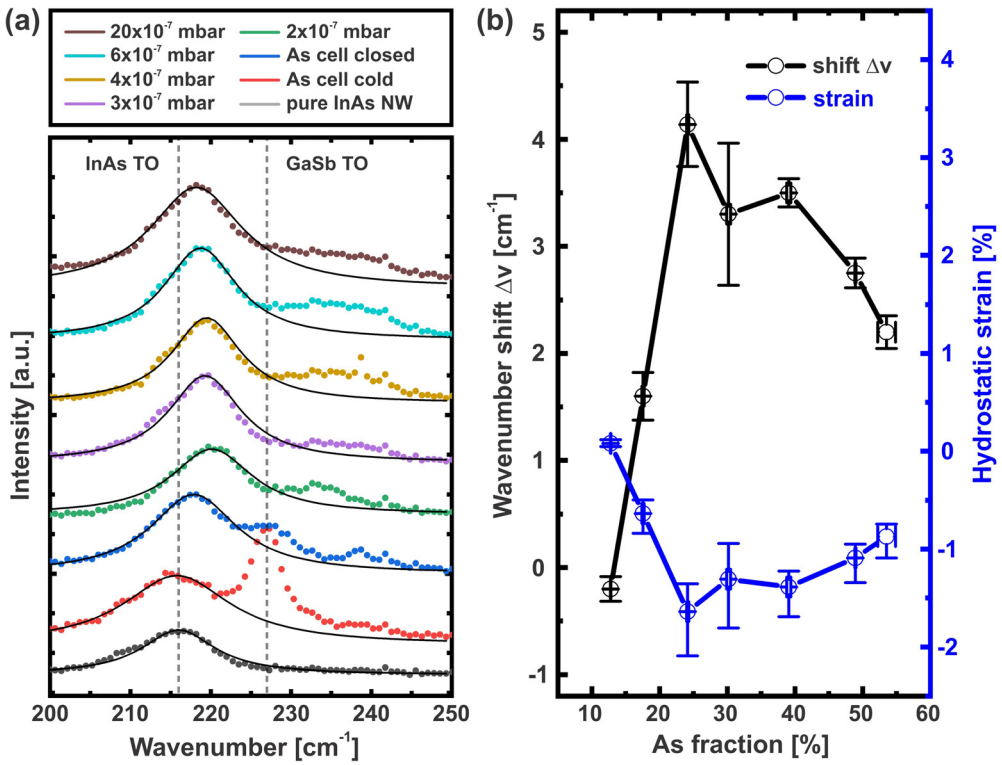

FIG. 3. (a) Raman spectra of the InAs TO-phonon mode shift of InAs–AlAsSb core–shell NWs in comparison to strain-free InAs NWs without shell (black data, InAs-TO: 216 cm^{-1}); (b) shifts of the peak wavenumber relative to strain-free InAs NWs ($\Delta\nu = 0$) and corresponding hydrostatic strain evolution as a function of the As-fraction in the AlAsSb shell.

mode, we directly extract the hydrostatic strain in the core using $\varepsilon_{hyd} = \varepsilon_{xx} + \varepsilon_{yy} + \varepsilon_{zz} \approx 1/\gamma_{TO} \cdot \Delta\nu/\nu_{TO}$, where $\gamma_{TO} = 1.17$ is the Grüneisen parameter describing the shift of the WZ-InAs TO phonons with hydrostatic strain.[44] This approximately linear relation holds true, since no peak splitting for the InAs TO phonons was found in our core-shell NWs. We further note that the relative peak shifts were attributed exclusively to strain without considering any other potential contributions, e.g., phonon confinement or zone-folding.[45]

Both the relative TO-mode shift and the corresponding change of hydrostatic strain in the InAs core are plotted in Fig. 3(b) as a function of AlAsSb shell composition. We clearly see that for the lowest As-fraction (13%), the InAs core experiences a weakly tensile strain (+0.08%), indicating that this shell composition is very close to lattice matching. Increasing the As-fraction changes the sign of strain, inducing compressive strain with values as high as −1.6% ([As] ∼ 25%). Further increase in the As-fraction results, however, in decreased compressive strain, despite the increased lattice mismatch. This suggests that partial strain relaxation sets in for As-fractions in excess of 30%, which was also proposed by the morphology transition to the 3D-grainlike structure in Fig. 1(b).

Ultimately, we probed the effect of strain on the bandgap of the InAs core using μPL spectroscopy on selected samples with low to moderate As-fractions (<30%). Measurements were performed in a home-built MIR-μPL setup on as-grown NW arrays as described in Refs. 27 and 46. Hereby, we used a continuous-wave laser diode at 975 nm for excitation that was focused onto the sample (spot size ∼13 μm), which was placed in a He-flow cryostat. The PL response was recorded by an InAs detector with the entire beam-path immersed in inert N_2 gas to prevent strong absorption from water in ambient air.[27] All presented PL spectra were taken at 10 K. Figure 4(a) shows normalized PL spectra from three investigated core–shell NW arrays in comparison with bare, unstrained InAs NWs recorded with an excitation power density of 8.7 kW/cm^2. The core-shell NWs contain InAs NW cores identical to the bare one but AlAsSb shells with different As fractions (13%, 18%, 25%, and 30%). According to the Raman data [Fig. 3(b)], the hydrostatic strain in these four samples corresponds to values of +0.08% (tensile), −0.63%, −1.64%, and −1.31% (compressive).

The emission of all samples was obtained in the range of ∼0.4–0.55 eV, suggesting that radiative recombination takes place primarily inside the InAs core, since AlAsSb is an indirect semiconductor with much larger bandgap. The bare, unstrained InAs NWs (black data) show a PL peak energy of ∼0.45 eV, which agrees well with former observations from WZ-phase InAs NWs grown under similar conditions.[27,46] For compressively strained InAs cores (AlAsSb shells with 18%, 25%, and 30%), the emission blue-shifts to larger energies with increasing As-fraction. This is expected, given the existence of compressive hydrostatic strain in the core that widens the bandgap. We further note that for all samples with a compressively strained core, the total integrated PL intensity is similarly high, confirming that the optical properties are not deteriorated upon increased As-fraction. In contrast, NWs with AlAsSb shell containing lower As-fraction (13%) show a very distinct red-shift with respect to the unstrained InAs core by ∼40 meV. In principle, such red-shift is expected under the presence of tensile strain in the core; however, the magnitude of the shift is quite large considering the very weak +0.08% tensile strain in this case.

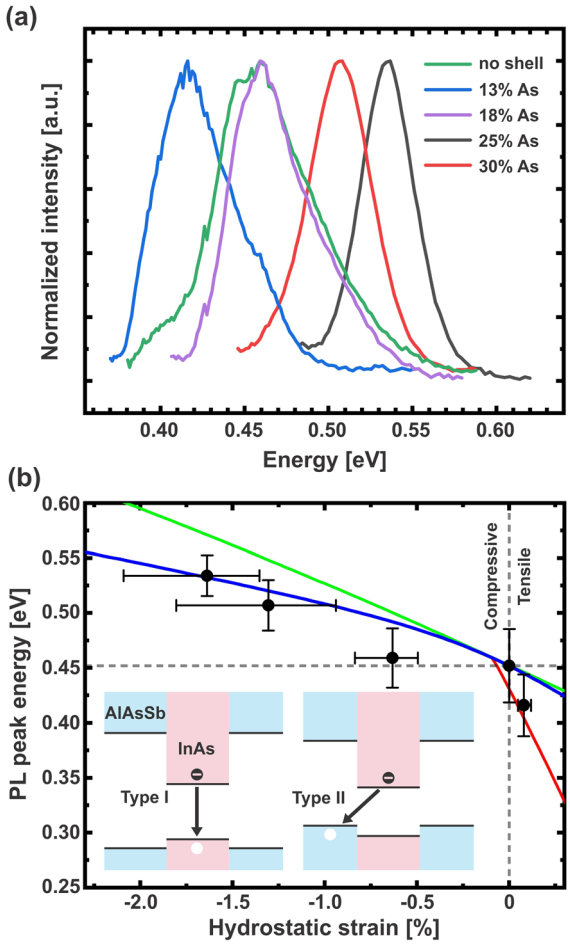

FIG. 4. (a) Normalized PL spectra of three InAs-AlAsSb core-shell NW arrays (different As-fractions in the shell) in comparison with a strain-free, bare InAs NW array as recorded at 10 K; (b) plot of the PL peak energy (black datapoints) as a function of the hydrostatic strain in the InAs core. For comparison, the calculated transition energies for direct type-I transitions (strain-dependent bandgap energy) as well as for indirect type-II transitions (red curve) are also shown. For type-I transitions, the bandgap energy is shown for two cases, averaged over the entire NW core (green curve) and as minimum bandgap energy (blue curve). The insets illustrate schematically the respective type-I and type-II band lineups and corresponding direct vs indirect transitions. (Band offsets are not to scale.)

To address this behavior more quantitatively, we plot in Fig. 4(b) the PL peak energies against the hydrostatic strain and compare our experimental data with calculations of the strain-induced changes in bandgap energy E_G based on theoretical calculations of WZ band-parameters[47] and deformation potentials of WZ InAs (see the supplementary material). Thereby, we employed the continuum elasticity theory (strain calculations) in combination with the $k \cdot p$ perturbation theory to compute the valence and conduction band edges and resulting minimum bandgap energy (see the supplementary material). We note that the minimum bandgap energy is located along the NW corner facets of the hexagonal core due to an enhanced splitting of the topmost valence bands, which results in a non-linear increase in the bandgap energy with hydrostatic strain [blue curve in Fig. 4(b)].

Looking at the compressive case (negative hydrostatic strain data), we find that the experimental data follow overall the trend of the calculated strain-induced bandgap shifts. Especially, for the sample with the highest compressive strain (25% As-fraction), the agreement is immaculate. This suggests that E_G can be attributed to near band edge transitions of electron–hole pairs within the compressively strained InAs core. This further supports the notion of a type-I band lineup between the InAs core and wide-gap AlAsSb shell (see the inset), as expected from the relatively large As-fraction. Note that the experimental data of the other two compressively strained samples fall slightly below the calculated bandgap energy. For the sample with largest As-fraction (30%), the deviation is a direct result of the apparent partial strain relaxation noted before. [The hydrostatic strain in this sample is lowered compared to the sample with As-fraction of 25% (cf. Fig. 3(b).] Regarding the deviation in the data of the sample with As-fraction of 18%, we believe this could be a result of the uncertainty in the InAs TO-mode positions and corresponding averaged hydrostatic strain in this sample, which has large effect in the limit of small overall strain.

For the case of weak tensile strain (positive hydrostatic strain), the calculated bandgap data suggest, in contrast, only a very small bandgap narrowing, i.e., ∼5 meV for $\varepsilon_{hyd} = 0.08\%$ (the sample with 13% AlAsSb). Here, however, the experimental data are far below the calculated bandgap, showing a red-shift of ∼40 meV. This huge red-shift can only be explained by taking a closer look at the band lineup of InAs-AlAsSb with low As-fraction and considering recombination involving the shell layer as well. In particular, we consider a type-II band lineup by which the relative position of the AlAsSb valence band (VB) shifts above the VB level of InAs, inducing spatially indirect recombination of electrons located in the InAs core and holes trapped in the adjacent AlAsSb shell interface (see the inset). To account for this, we further calculated the strain-(i.e., composition) dependent type-II transition energy (see the red line), which changes much more rapidly with strain as opposed to the type-I transition, i.e., the transition energy drops over several tens of meV even for miniscule change in strain <0.1%. Remarkably, the experimental data (the PL energy of ∼0.415 eV) fit very well with the calculated indirect transition, reflecting the apparent type-II band lineup for such InAs-AlAsSb core-shell NWs with low As-fraction. Similar type-II band lineup was recently also proposed for a binary AlSb passivation layer on InAs NWs, but without electronic structure calculations only qualitative assumptions could be made.[29] Moreover, our findings of a type-II transition with low emission energy for such low As-fraction AlAsSb and small strain mimic very well previous observations of planar InAs-AlAsSb heterostructures.[48,49]

See the supplementary material for additional Raman spectroscopy data, high-resolution and scanning transmission electron microscopy analysis, and simulations of strain-induced bandgap shifts.

This work was supported financially by the Deutsche Forschungsgemeinschaft (DFG) via Project Grant No. KO-4005/10-1 and via Germany's Excellence Strategy-EXC2089/1-390776260 (e-conversion). Further support was provided by the European Research Council (ERC project QUANtIC, ID: 771747), the International Graduate School of Science and Engineering (TUM-IGSSE), and the TUM Institute for Advanced Study (IAS) via the Focal Periods Program 2019. The authors also thank A. Holleitner and the Center for Nanotechnology and Nanomaterials (ZNN) for experimental support.

AUTHOR DECLARATIONS

Conflict of Interest

The authors have no conflicts to disclose.

DATA AVAILABILITY

The data that support the findings of this study are available from the corresponding author upon reasonable request.

REFERENCES

[1]T. Bryllert, L.-E. Wernersson, L. Froberg, and L. Samuelson, "Vertical high-mobility wrap-gated InAs nanowire transistor," IEEE Electron Device Lett. **27**, 323–325 (2006).
[2]S. Dayeh, D. P. Aplin, X. Zhou, P. K. Yu, E. Yu, and D. Wang, "High electron mobility InAs nanowire field-effect transistors," Small **3**, 326–332 (2007).
[3]Y. Tian, M. R. Sakr, J. M. Kinder, D. Liang, M. J. MacDonald, R. L. J. Qiu, H.-J. Gao, and X. P. A. Gao, "One-dimensional quantum confinement effect modulated thermoelectric properties in InAs nanowires," Nano Lett. **12**, 6492–6497 (2012).
[4]P. M. Wu, J. Gooth, X. Zianni, S. F. Svensson, J. G. Gluschke, K. A. Dick, C. Thelander, K. Nielsch, and H. Linke, "Large thermoelectric power factor enhancement observed in InAs nanowires," Nano Lett. **13**, 4080–4086 (2013).
[5]X. Zhang, H. Huang, X. Yao, Z. Li, C. Zhou, X. Zhang, P. Chen, L. Fu, X. Zhou, J. Wang, W. Hu, W. Lu, J. Zou, H. H. Tan, and C. Jagadish, "Ultrasensitive mid-wavelength infrared photodetection based on a single InAs nanowire," ACS Nano **13**, 3492–3499 (2019).
[6]A. Alhodaib, Y. J. Noori, P. J. Carrington, A. M. Sanchez, M. D. Thompson, R. J. Young, A. Krier, and A. R. J. Marshall, "Room-temperature mid-infrared emission from faceted InAsSb multi quantum wells embedded in InAs nanowires," Nano Lett. **18**, 235–240 (2018).
[7]H. Sumikura, G. Zhang, M. Takiguchi, N. Takemura, A. Shinya, H. Gotoh, and M. Notomi, "Mid-infrared lasing of single wurtzite InAs nanowire," Nano Lett. **19**, 8059–8065 (2019).
[8]A. Arlauskas, J. Treu, K. Saller, I. Beleckaite, G. Koblmüller, and A. Krotkus, "Strong terahertz emission and its origin from catalyst-free InAs nanowire arrays," Nano Lett. **14**, 1508–1514 (2014).
[9]H. Lin, Z. Luo, T. Gu, L. C. Kimerling, K. Wada, A. Agarwal, and J. Hu, "Mid-infrared integrated photonics on silicon: A perspective," Nanophotonics **7**, 393–420 (2017).
[10]E. Delli, P. D. Hodgson, M. Bentley, E. Repiso, A. P. Craig, Q. Lu, R. Beanland, A. R. J. Marshall, A. Krier, and P. J. Carrington, "Mid-infrared type-II InAs/InAsSb quantum wells integrated on silicon," Appl. Phys. Lett. **117**, 131103 (2020).
[11]M. Speckbacher, J. Treu, T. J. Whittles, W. M. Linhart, X. Xu, K. Saller, V. R. Dhanak, G. Abstreiter, J. J. Finley, T. D. Veal, and G. Koblmüller, "Direct measurements of fermi level pinning at the surface of intrinsically n-type InGaAs nanowires," Nano Lett. **16**, 5135–5142 (2016).
[12]G. W. Holloway, Y. Song, C. M. Haapamaki, R. R. LaPierre, and J. Baugh, "Electron transport in InAs–InAlAs core–shell nanowires," Appl. Phys. Lett. **102**, 043115 (2013).
[13]X. Li, K. Zhang, J. Treu, L. Stampfer, G. Koblmüller, F. Toor, and J. P. Prineas, "Contactless optical characterization of carrier dynamics in free-standing InAs–InAlAs core–shell nanowires on silicon," Nano Lett. **19**, 990–996 (2019).
[14]J. Treu, M. Bormann, H. Schmeiduch, M. Döblinger, S. Morkötter, S. Matich, P. Wiecha, K. Saller, B. Mayer, M. Bichler, M.-C. Amann, J. J. Finley, G. Abstreiter, and G. Koblmüller, "Enhanced luminescence properties of InAs–InAsP core–shell nanowires," Nano Lett. **13**, 6070–6077 (2013).
[15]D. Ren, K. M. Azizur-Rahman, Z. Rong, B.-C. Juang, S. Somasundaram, M. Shahili, A. C. Farrell, B. S. Williams, and D. L. Huffaker, "Room-temperature midwavelength infrared InAsSb nanowire photodetector arrays with Al_2O_3 passivation," Nano Lett. **19**, 2793–2802 (2019).

[16]P. Jurczak, Y. Zhang, J. Wu, A. M. Sanchez, M. Aagesen, and H. Liu, "Ten-fold enhancement of InAs nanowire photoluminescence emission with an InP passivation layer," Nano Lett. **17**, 3629–3633 (2017).
[17]C. M. Haapamaki, J. Baugh, and R. R. LaPierre, "Critical shell thickness for InAs-$Al_xIn_{1-x}As$(p) core-shell nanowires," J. Appl. Phys. **112**, 124305 (2012).
[18]P. Schmiedeke, A. Thurn, S. Matich, M. Döblinger, J. J. Finley, and G. Koblmüller, "Low-threshold strain-compensated InGaAs/(In, Al)GaAs multi-quantum well nanowire lasers emitting near 1.3 m at room temperature," Appl. Phys. Lett. **118**, 221103 (2021).
[19]E. Nakai, M. Yoshimura, K. Tomioka, and T. Fukui, "GaAs/InGaP core–multishell nanowire-array-based solar cells," Jpn. J. Appl. Phys., Part 1 **52**, 055002 (2013).
[20]S. Morkötter, N. Jeon, D. Rudolph, B. Loitsch, D. Spirkoska, E. Hoffmann, M. Döblinger, S. Matich, J. J. Finley, L. J. Lauhon, G. Abstreiter, and G. Koblmüller, "Demonstration of confined electron gas and steep-slope behavior in delta-doped GaAs-AlGaAs core–shell nanowire transistors," Nano Lett. **15**, 3295–3302 (2015).
[21]G. G. Zegrya and A. D. Andreev, "Mechanism of suppression of auger recombination processes in type-II heterostructures," Appl. Phys. Lett. **67**, 2681–2683 (1995).
[22]A. M. Hoang, G. Chen, R. Chevallier, A. Haddadi, and M. Razeghi, "High performance photodiodes based on InAs/InAsSb type-II superlattices for very long wavelength infrared detection," Appl. Phys. Lett. **104**, 251105 (2014).
[23]H. Esmaielpour, V. R. Whiteside, J. Tang, S. Vijeyaragunathan, T. D. Mishima, S. Cairns, M. B. Santos, B. Wang, and I. R. Sellers, "Suppression of phonon-mediated hot carrier relaxation in type-II InAs/$AlAs_xSb_{1-x}$ quantum wells: A practical route to hot carrier solar cells," Prog. Photovoltaics: Res. Appl. **24**, 591–599 (2016).
[24]H. Kroemer, "The family (InAs, GaSb, AlSb) and its heterostructures: A selective review," Physica E **20**, 196–203 (2004).
[25]S. Hertenberger, D. Rudolph, M. Bichler, J. J. Finley, G. Abstreiter, and G. Koblmüller, "Growth kinetics in position-controlled and catalystfree InAs nanowire arrays on Si(111) grown by selective area molecular beam epitaxy," J. Appl. Phys. **108**, 114316 (2010).
[26]F. del Giudice, J. Becker, C. de Rose, M. Döblinger, D. Ruhstorfer, L. Suomenniemi, J. Treu, H. Riedl, J. J. Finley, and G. Koblmüller, "Ultrathin catalyst-free InAs nanowires on silicon with distinct 1d sub-band transport properties," Nanoscale **12**, 21857–21868 (2020).
[27]S. Morkötter, S. Funk, M. Liang, M. Doblinger, S. Hertenberger, J. Treu, D. Rudolph, A. Yadav, J. Becker, M. Bichler, G. Scarpa, P. Lugli, I. Zardo, J. J. Finley, G. Abstreiter, and G. Koblmüller, "Role of microstructure on optical properties in high-uniformity $In_{1-x}Ga_xAs$ nanowire arrays: Evidence of a wider wurtzite band gap," Phys. Rev. B **87**, 205303 (2013).
[28]D. Ruhstorfer, A. Lang, S. Matich, M. Döblinger, H. Riedl, J. J. Finley, and G. Koblmüller, "Growth dynamics and compositional structure in periodic InAsSb nanowire arrays on Si(111) grown by selective area molecular beam epitaxy," Nanotechnology **32**, 135604 (2021).
[29]H. Li, H. Alradhi, Z. Jin, E. A. Anyebe, A. M. Sanchez, W. M. Linhart, R. Kudrawiec, H. Fang, Z. Wang, W. Hu, and Q. Zhuang, "Novel type-II InAs/AlSb core–shell nanowires and their enhanced negative photocurrent for efficient photodetection," Adv. Funct. Mater. **28**, 1705382 (2018).
[30]H. Kindlund, R. R. Zamani, A. R. Persson, S. Lehmann, L. R. Wallenberg, and K. A. Dick, "Kinetic engineering of wurtzite and zinc-blende AlSb shells on InAs nanowires," Nano Lett. **18**, 5775–5781 (2018).
[31]D. Rudolph, S. Funk, M. Doblinger, S. Morkötter, S. Hertenberger, L. Schweickert, J. Becker, S. Matich, M. Bichler, D. Spirkoska, I. Zardo, J. J. Finley, G. Abstreiter, and G. Koblmüller, "Spontaneous alloy composition ordering in GaAs-AlGaAs core–shell nanowires," Nano Lett. **13**, 1522–1527 (2013).
[32]A. Hirai, B. A. Haskell, M. B. McLaurin, F. Wu, M. C. Schmidt, K. C. Kim, T. J. Baker, S. P. DenBaars, S. Nakamura, and J. S. Speck, "Defect-mediated surface morphology of nonpolar m-plane GaN," Appl. Phys. Lett. **90**, 121119 (2007).
[33]G. Koblmüller, A. Hirai, F. Wu, C. S. Gallinat, G. D. Metcalfe, H. Shen, M. Wraback, and J. S. Speck, "Molecular beam epitaxy and structural anisotropy of m-plane InN grown on free-standing GaN," Appl. Phys. Lett. **93**, 171902 (2008).
[34]L. Lymperakis and J. Neugebauer, "Large anisotropic adatom kinetics on non-polar GaN surfaces: Consequences for surface morphologies and nanowire growth," Phys. Rev. B **79**, 241308 (2009).
[35]N. G. Hormann, I. Zardo, S. Hertenberger, S. Funk, S. Bolte, M. Döblinger, G. Koblmüller, and G. Abstreiter, "Effects of stacking variations on the lattice dynamics of InAs nanowires," Phys. Rev. B **84**, 155301 (2011).
[36]M. Möller, M. M. de Lima, A. Cantarero, L. C. O. Dacal, J. R. Madureira, F. Iikawa, T. Chiaramonte, and M. A. Cotta, "Polarized and resonant Raman spectroscopy on single InAs nanowires," Phys. Rev. B **84**, 085318 (2011).
[37]Z. Algarni, A. Singh, and U. Philipose, "Synthesis of amorphous InSb nanowires and a study of the effects of laser radiation and thermal annealing on nanowire crystallinity," Nanomaterials **8**, 607 (2018).
[38]R. Ferrini, M. Galli, G. Guizzetti, M. Patrini, A. Bosacchi, S. Franchi, and R. Magnanini, "Phonon response of$Al_xGa_{1-x}Sb$/GaSbepitaxial layers by Fourier-transform infrared-reflectance and Raman spectroscopies," Phys. Rev. B **56**, 7549 (1997).
[39]G. Lucovsky, K. Y. Cheng, and G. L. Pearson, "Study of the long-wavelength optic phonons in$Ga_{1-x}Al_xSb$," Phys. Rev. B **12**, 4135–4141 (1975).
[40]I. Sela, C. R. Bolognesi, and H. Kroemer, "Single-mode behavior of$AlSb_{1-x}As_x$ alloys," Phys. Rev. B **46**, 16142–16143 (1992).
[41]H. Lin, J. Ou, C. Hsu, W. Chen, and M. Lee, "Raman scattering in ternary $AlAs_xSb_{1-x}$ films," Solid State Commun. **107**, 547–551 (1998).
[42]S. Hertenberger, S. Funk, K. Vizbaras, A. Yadav, D. Rudolph, J. Becker, S. Bolte, M. Döblinger, M. Bichler, G. Scarpa, P. Lugli, I. Zardo, J. J. Finley, M.-C. Amann, G. Abstreiter, and G. Koblmüller, "High compositional homogeneity in in-rich InGaAs nanowire arrays on nanoimprinted SiO_2/Si (111)," Appl. Phys. Lett. **101**, 043116 (2012).
[43]K. R. Evans, "Mass-spectrometric determination of antimony incorporation during III–V molecular beam epitaxy," J. Vac. Sci. Technol. B **8**, 271 (1990).
[44]S. Yazji, I. Zardo, S. Hertenberger, S. Morkötter, G. Koblmüller, G. Abstreiter, and P. Postorino, "Pressure dependence of Raman spectrum in InAs nanowires," J. Phys.: Condens. Matter **26**, 235301 (2014).
[45]K. Aoki, E. Anastassakis, and M. Cardona, "Dependence of Raman frequencies and scattering intensities on pressure in GaSb, InAs, and InSb semiconductors," Phys. Rev. B **30**, 681–687 (1984).
[46]M. Sonner, J. Treu, K. Saller, H. Riedl, J. J. Finley, and G. Koblmüller, "Carrier concentration dependent photoluminescence properties of Si-doped InAs nanowires," Appl. Phys. Lett. **112**, 091904 (2018).
[47]F. Bechstedt and A. Belabbes, "Structure, energetics, and electronic states of III–V compound polytypes," J. Phys.: Condens. Matter **25**, 273201 (2013).
[48]V. R. Whiteside, B. A. Magill, M. P. Lumb, H. Esmaielpour, M. A. Meeker, R. H. Mudiyanselage, A. Messager, S. Vijeyaragunathan, T. D. Mishima, M. B. Santos, I. Vurgaftman, G. A. Khodaparast, and I. R. Sellers, "Valence band states in an InAs/AlAsSb multi-quantum well hot carrier absorber," Semicond. Sci. Technol. **34**, 025005 (2019).
[49]H. P. Piyathilaka, R. Sooriyagoda, H. Esmaielpour, V. R. Whiteside, T. D. Mishima, M. B. Santos, I. R. Sellers, and A. D. Bristow, "Hot-carrier dynamics in InAs/AlAsSb multiple-quantum wells," Sci. Rep. **11**, 10483 (2021).